

1     **Response of the East Asian Summer Monsoon to Atmospheric**  
2            **CO<sub>2</sub> Forcing and Subsequent Sea Surface Warming**

3                    **JINQIANG CHEN \* AND SIMONA BORDONI**

*California Institute of Technology, Pasadena, California*

---

\* *Corresponding author address:* Jinqiang Chen, California Institute of Technology, 1200 E. California Blvd. M.C.131-24, Pasadena, CA 91125.  
E-mail: jchen@gps.caltech.edu

## ABSTRACT

4  
5 The regional climate change of the East Asian summer monsoon (EASM) is investigated in  
6 the Coupled Model Intercomparison Project – Phase 5 (CMIP5) archive. In the greenhouse  
7 gas forced scenario, reduction of radiative cooling and increase in continental surface temper-  
8 ature occur much more rapidly than changes in sea surface temperatures (SSTs). Without  
9 changes in SSTs, the rainfall in the monsoon region decreases (increases) over ocean (land)  
10 in most models. On longer time scales, as SSTs increase, rainfall changes are opposite. The  
11 total response to atmospheric CO<sub>2</sub> forcing and subsequent SST warming is a large (mod-  
12 est) increase in rainfall over ocean (land) in the EASM region. Dynamic changes, in spite  
13 of significant contributions from the thermodynamic component, play an important role in  
14 setting up the spatial pattern of precipitation changes. Rainfall anomalies over East China  
15 are a direct consequence of local land-sea contrast, while changes in the larger-scale oceanic  
16 rainfall band are closely associated with the displacement of the larger-scale North Pacific  
17 Subtropical High (NPSH). Ad hoc numerical simulations with the AM2.1 general circulation  
18 model show that topography and SST patterns play an important role in rainfall changes in  
19 the EASM region.

# 1. Introduction

It is well understood that the increase in global precipitation in response to greenhouse warming is energetically constrained rather than being limited by the availability of atmospheric water vapor (e.g., Mitchell et al. 1987; O’Gorman et al. 2012). Therefore, global precipitation changes less rapidly with temperature (at around 2%  $\text{K}^{-1}$  in current climate) than the change in water vapor in the atmosphere at around 7.5%  $\text{K}^{-1}$  from the Clausius-Clapeyron relation (Held and Soden 2006). Changes in precipitation at the regional scale are more complex, and arguably more important than global changes, as circulation changes will affect the precipitation locally. Here, we explore regional changes in the East Asian summer monsoon (EASM) region, in response to  $\text{CO}_2$  forcing. Although it has been found that the rainfall during the EASM season is projected to increase at the end of the 21<sup>st</sup> century, limited understanding has prevented us from robustly identifying the physical and dynamical processes contributing to the change of the EASM and from better constraining the inter-model spread of EASM projections. Understanding how the EASM responds to a changing climate can provide support to theories of its maintenance in present-day climate and shed light into the dynamics and responses of other subtropical convergence zones to climate change.

The mechanisms that alter regional precipitation vary at different time scales. A fast response to an increase in  $\text{CO}_2$  concentration before sea surface temperatures (SSTs) change occurs at short timescales and is associated with changes in large-scale wind patterns in the atmosphere. Large uncertainties in the precipitation change are found in the fast response, particularly over tropical oceanic regions, which are identified as a primary contributor to the inter-model spread in the difference in simulated precipitation between two equilibrium climate states (Bony et al. 2013). A slow response to the subsequent increase in SSTs while maintaining the  $\text{CO}_2$  concentration fixed in the atmosphere is found to resemble the climatological precipitation pattern following the “wet get wetter” behavior (Held and Soden 2006).

47 The “wet get wetter” response captures the thermodynamic response of net rainfall over  
48 oceanic regions to SST forcing. Based on the assumptions of unchanged relative humidity  
49 and circulation, increases in atmospheric water vapor in a warmer climate intensify clima-  
50 tological convergence of water vapor fluxes. As a result, climatological wet regions (positive  
51 net precipitation regions) will become wetter, and climatological dry regions (negative net  
52 precipitation regions) will become drier. This simplified depiction has been generally accept-  
53 ed in the study of the response of the hydrological cycle to climate change; however, because  
54 of its assumptions, it does not capture the complexity of the thermodynamic precipitation  
55 response at the regional scale. For example, Xie et al. (2010) found that tropical rainfall  
56 change follows a “warmer get wetter” pattern modulated by future SST pattern, rather than  
57 the “wet get wetter” pattern, which can only be realized if SSTs are increased uniformly.

58 While providing a useful starting point, the thermodynamic change due to SSTs is only  
59 one component of the total precipitation response. Dynamic changes in response to SST  
60 forcing have also been found to be important both globally and locally (e.g., Xie et al. 2010,  
61 2009; He and Zhou 2015). Over the EASM region, dynamic changes have, for instance,  
62 shown to be associated with changes in the North Pacific subtropical high (NPSH). Kitoh  
63 et al. (1997) found that global warming is associated with a strengthening and southward  
64 movement of the NPSH in a global climate model (GCM). Together with more El Niño-like  
65 patterns in future climates, it explains the mean sea-level pressure anomalies that might be  
66 related to the delay of Baiu withdrawal simulated in GCMs (Kitoh and Uchiyama 2006). The  
67 influence of tropical SST anomalies on the western NPSH has been vastly explored at the  
68 interannual timescale. It has been proposed that increases in rainfall over the tropical Indian  
69 Ocean due to the resulting warm SST anomalies from El Niño in the precedent year generate  
70 Kelvin waves emanating into the tropical western Pacific, inducing local northeasterly surface  
71 wind anomalies and resulting in an anticyclonic circulation over the western North Pacific  
72 (e.g., Yang et al. 2007; Xie et al. 2009). This signal can be enhanced by a cold tropical Pacific  
73 SST anomaly that generates anticyclonic Rossby waves to its northwestern region (e.g., Terao

74 and Kubota 2005). This relationship between the western NPSH and the zonal SST gradient  
75 between the tropical Indian Ocean and the tropical Western Pacific is examined in RCP4.5  
76 and RCP8.5 model outputs in CMIP5 by He and Zhou (2015). They found that this zonal  
77 temperature gradient has a robust influence on simulated western NPSH anomalies, which  
78 modulate the climate change over eastern China. In addition, they performed a sensitivity  
79 test on the impact of tropical SST anomalies on the western NPSH, and they showed that  
80 both the tropical Indian Ocean and tropical Western Pacific SST anomalies contribute to  
81 changes in the projected western NPSH intensity.

82 Mechanisms driven by changes other than just SSTs have, however, been invoked. Zhao  
83 et al. (2011a) investigated the tropical-North Pacific mode in present climate and found  
84 that this mode is closely correlated with the variability of climate over Asia and the Pacific  
85 Ocean through Asian-Pacific Oscillation (APO). Sensitivity experiments emphasize the  
86 importance of the Asian land heating due to the Tibetan Plateau (the TP) in generating  
87 summertime Asian-Pacific climate anomalies. Pacific SST forcing, seemingly important in  
88 this teleconnection, was suggested to play a much weaker role in the summertime Asian-  
89 Pacific atmospheric circulation. At interdecadal timescale, Zhao et al. (2011b) found that  
90 from a low-APO to a high-APO decade, both the upper-tropospheric SAH and the lower-  
91 tropospheric low pressure system intensify over Asia. This strengthened circulation results  
92 in anomalous southerly, southwesterly winds prevailing over the Asian monsoon region and  
93 leads to a strong northward transport of moisture and enhanced rainfall over the Asian  
94 monsoon region.

95 In this paper, we investigate the response of the EASM to CO<sub>2</sub> forcing at different  
96 timescales, and untangle various dynamic and thermodynamic processes that can mediate  
97 the precipitation response to changes in boundary forcing (such as land-sea contrast, topog-  
98 raphy and SSTs) through radiation-circulation interactions. Specifically, we ask: What are  
99 the mechanisms of EASM rainfall changes and spread amongst CMIP5 models at different  
100 (fast and slow) time scales? To provide answers to this question, we leverage numerical exper-

101 iments with state-of-the-art climate models in the CMIP5 archive. Additional experiments  
102 are performed with the Geophysical Fluid Dynamics Laboratory (GFDL) Atmospheric Mod-  
103 el, version 2.1 (AM2.1, Anderson et al. (2004)) to further investigate mechanisms. In section  
104 2, we briefly describe the data and methods used in this study. In section 3, we present  
105 results from investigation of CMIP5 experiments. Additional experiments performed ad hoc  
106 are discussed in section 4. Discussion and conclusions are provided in section 5.

## 107 **2. Data and Method**

108 We use 11 climate model single realization outputs (Table 1) with monthly mean from  
109 several CMIP5 experiments (Taylor et al. 2012): 30-year atmosphere-only simulations forced  
110 by a fixed 1xCO<sub>2</sub> or 4xCO<sub>2</sub> concentration with prescribed SST distribution that remains  
111 unchanged in both sets of experiments (sstClim or sstClim4xCO<sub>2</sub>); 150-year fully-coupled  
112 ocean-atmosphere simulations forced by a constant 4xCO<sub>2</sub> concentration (abrupt4xCO<sub>2</sub>);  
113 and fully-coupled simulations forced by pre-industrial forcings (piControl). The 30-year  
114 sstClim and sstClim4xCO<sub>2</sub>, piControl and the last 30 years of abrupt4xCO<sub>2</sub> are averaged  
115 to represent the climatology of different climate states. The monthly resolution of available  
116 data does not allow for consideration of sub-monthly transient eddies in our analyses.

117 The fast response is computed as the difference between sstClim4xCO<sub>2</sub> and sstClim, in  
118 which the SST distribution is prescribed based on the climatology from pre-industrial simula-  
119 tions. In these two sets of experiments the only difference is, therefore, the atmospheric CO<sub>2</sub>  
120 concentration. The slow response is computed as the difference between abrupt4xCO<sub>2</sub> and  
121 sstClim4xCO<sub>2</sub>, in which the atmospheric CO<sub>2</sub> concentration in both scenarios is essentially  
122 the same, and the only difference is the subsequent warming in SSTs in the abrupt4xCO<sub>2</sub>  
123 scenario.

124 As done in several previous studies of regional climate changes, we use the moisture  
125 budget to study the hydrological change in the EASM region,

$$\langle \overline{\partial_t q} \rangle + \langle \overline{\nabla \cdot (\mathbf{v}q)} \rangle + \langle \overline{\partial_p(\omega q)} \rangle = -\overline{P} + \overline{E}, \quad (1)$$

126 where  $\mathbf{v}$  indicates horizontal winds,  $\omega$  is vertical wind,  $q$  is water vapor in the atmosphere,  
 127  $P$  is precipitation, and  $E$  is evaporation.  $\overline{(\cdot)}$  indicates temporal mean. Ignoring water vapor  
 128 storage in the atmosphere and vertical velocity at the surface, Eq. 1 can be written as

$$\overline{P} - \overline{E} = -\langle \overline{\nabla \cdot (\mathbf{v}q)} \rangle. \quad (2)$$

129 This budget closes only if variables  $\mathbf{v}$  and  $q$  include all temporal resolutions. Because our  
 130 data are at monthly resolution, the calculated moisture flux convergence does not include  
 131 the contribution from sub-monthly transient eddies. Hence, this contribution has to be  
 132 estimated as the residual of Eq. 2. In the following, we will drop the notation  $\overline{(\cdot)}$ , with all  
 133 variables in following equations indicating monthly means.

134 In order to expose contributions from individual climatic variables to changes in the  
 135 moisture budget, we decompose specific humidity,  $q$ , into the product of relative humidity,  
 136  $H$ , and saturation specific humidity,  $q_s$ , as done by previous studies. One caveat is that  
 137 by using the monthly average of relative humidity, we ignore the covariance of relative  
 138 humidity and temperature (through the saturation specific humidity) on frequencies higher  
 139 than monthly.

140 The moisture budget can hence be written as

$$\delta(P - E) = -\langle \delta \nabla \cdot (\mathbf{v} \cdot H q_s) \rangle + \text{residual}, \quad (3)$$

141 where  $\delta$  indicates the difference between sstClim4xCO2 and sstClim (abrupt4xCO2 and  
 142 sstClim4xCO2) scenarios in the fast (slow) response, and the second term on the right hand  
 143 side of Eq. 3 is a residual, including sub-monthly transient eddies and moisture tendency in

144 the atmosphere. The moisture flux convergence term can be further decomposed as,

$$\begin{aligned}
-\langle \delta \nabla \cdot (\mathbf{v} \cdot H q_s) \rangle &= -\langle \nabla \cdot (\delta \mathbf{v} \cdot H q_s(T)) \rangle + \\
&\quad -\langle \nabla \cdot (\mathbf{v} \cdot q_s(T) \delta H) \rangle - \langle \nabla \cdot (\mathbf{v} \cdot H \delta q_s(T)) \rangle - \langle \nabla \cdot (\mathbf{v} \cdot \delta H \delta q_s(T)) \rangle + \\
&\quad -\langle \nabla \cdot (\delta \mathbf{v} \cdot q_s(T) \delta H) \rangle - \langle \nabla \cdot (\delta \mathbf{v} \cdot H \delta q_s(T)) \rangle - \langle \nabla \cdot (\delta \mathbf{v} \cdot \delta H \delta q_s(T)) \rangle,
\end{aligned}
\tag{4}$$

145 where terms on the right hand side represent, respectively, the change due to winds, rela-  
146 tive humidity, saturation specific humidity and hence temperature, the covariance between  
147 relative humidity and temperature, the covariance between winds and relative humidity, the  
148 covariance between winds and temperature and the covariance among winds, temperature,  
149 and relative humidity. Assuming no changes in winds and relative humidity, anomalies due  
150 to saturation specific humidity,  $-\langle \nabla(\mathbf{v} \cdot H \delta q_s(T)) \rangle$ , can be further decomposed into two  
151 terms,  $-\langle \nabla(\mathbf{v} \cdot H \delta q_s^*(T)) \rangle$  and  $-\langle \nabla(\mathbf{v} \cdot H \delta(q_s(T) - q_s^*(T))) \rangle$ , where  $q_s^*(T)$  is  $q_s(T)$  at the  
152 surface. The former can also be written as  $-\alpha \delta T(P - E)$ , where  $\alpha = L_v/RT^2$ ,  $L_v$  is the  
153 latent heat of evaporation and  $R$  is the gas constant for water vapor.  $-\alpha \delta T(P - E)$  has  
154 been described in the literature as the “wet get wetter” pattern (e.g., Held and Soden 2006),  
155 by assuming fixed shape of the temperature profile under climate change (similar to the  
156 Planck response in climate sensitivity studies) and ignoring changes in transient eddy fluxes.  
157 It predicts that with warming,  $\delta T$ , the pattern of net precipitation ( $P - E$ ) will simply be  
158 enhanced: becoming more positive when it is already positive; and more negative when it is  
159 already negative. The latter arises due to lapse rate changes or changes in the shape of the  
160 temperature profile.

161 In addition to these CMIP5 experiments, we also perform simulations with the GFDL  
162 AM2.1. Six experiments (noTopo\_control, noTopo\_4xCO2, Topo\_control, Topo\_4xCO2, U-  
163 ni4K and CMIP5SST) are performed (see more details in Table 2). These experiments have  
164 been designed to explore the impact of different regional forcings, such as land-sea con-  
165 trast, topography and SST distribution, on the EASM response. For instance, the difference  
166 between noTopo\_4xCO2 and noTopo\_control is expected to show how enhanced land-sea

167 thermal contrast influences regional precipitation without any contribution from topograph-  
168 ic forcing. These results can be compared with their counterparts with full topography. The  
169 difference between 4xCO<sub>2</sub> and Uni4K or CMIP5SST is expected to show how SST patterns  
170 (in addition to SST uniform warming) affect the EASM. Climatological-fixed SSTs without  
171 internannual variability from monthly-mean Reynolds SST analysis are used as boundary  
172 condition (Smith et al. 1996). Each experiment ran for 25 years, and the last 14 years of the  
173 simulations are used for the analyses.

174 We analyze changes in the EASM precipitation and circulation just for the month of  
175 June, when most models well capture the EASM rainfall band. In doing so, we ignore  
176 possible changes in the EASM seasonality and only focus on seasonal mean changes in  
177 rainfall intensity and position.

### 178 **3. Rainfall anomalies**

179 With quadruple CO<sub>2</sub> forcing, rainfall increases over the EASM region, particularly over  
180 the oceanic regions on the southern flank of the rainfall band (Fig. 1a). Most of the precip-  
181 itation increase only happens when SST starts to warm. With CO<sub>2</sub> forcing alone, rainfall  
182 decreases over oceanic regions, while it increases over East China (Fig. 1b). The decrease in  
183 precipitation is colocated with the rainfall band, indicating that it is not simply a result of  
184 model artifact but a robust signal in changes in the strength of the EASM precipitation. The  
185 slow response shows a pattern opposite to the fast response – rainfall decreases over East  
186 China while it increases over the oceanic regions (Fig. 1d). The difference between coupled  
187 and uncoupled simulations in EASM precipitation is fairly small (Fig. 1c, the spatial pat-  
188 tern and magnitude is consistent with a recent study by Song and Zhou 2014, their Fig. 8c)  
189 compared to that in either fast or slow response, allowing us to safely conclude that air-sea  
190 interaction can be ignored and that the signal in Fig. 1d comes from the SST forcing in the  
191 MMM.

192 *a. Fast Response*

193 The fast response of the EASM rainfall band to elevated CO<sub>2</sub> concentrations with fixed  
194 SSTs features a decrease (increase) of precipitation over oceanic (land) regions (Fig. 1b).  
195 This precipitation response is robust in most models (not shown).

196 Anomalies in net precipitation (Fig. 2a) largely explain the pattern of precipitation  
197 change in the EASM (Fig. 1b), with changes in evaporation being important only over oceanic  
198 regions: here, the contribution by evaporation decreases along regions of large climatological  
199 evaporation (Fig. 2b). The spatial pattern of net precipitation change is consistent with  
200 changes in mean moisture flux convergence (Fig. 2c), although transient eddy flux anoma-  
201 lies, calculated as the residual of the moisture budget, are not negligible (Fig. 2d). Changes  
202 in mean moisture flux convergence are mainly captured by those due to winds (Fig. 2e).  
203 Contributions from changes in temperature (Fig. 2g), relative humidity (Fig. 2f), and their  
204 covariances (Fig. 2j-l) play a less important role. This confirms that in the absence of SST  
205 changes, the precipitation response is primarily dominated by changes in circulation, as seen  
206 in other tropical-subtropical regions (Bony et al. 2013).

207 *b. Slow response*

208 At a first glance, changes in the slow response appear to follow the “wet get wetter” pat-  
209 tern. However, important deviations from the simple thermodynamic change exist (Fig. 3a):  
210 While the response is characterized by a well organized positive change in net precipitation,  
211 this is located to the south of its climatological location. The net precipitation change over  
212 East China is negative, counteracting its positive change in the fast response. Surface evap-  
213 oration increases, particularly over oceanic regions where large evaporation reductions occur  
214 in the fast response (Fig. 3b). This increase in surface evaporation might be due to the  
215 experiment configuration: in *sstClim4xCO2*, SSTs are prescribed and surface evaporation is  
216 strongly limited; in *abrupt4xCO2*, SSTs are interactive, and a strong increase in local SSTs

217 due to ocean dynamics might explain the narrow band of enhanced evaporation (Xie et al.  
218 2010).

219 The mean flux convergence,  $-\langle\delta\nabla(\mathbf{v}\cdot Hq_s)\rangle$ , captures the overall spatial pattern of the  
220 net precipitation change in Fig. 3a, with strong moisture convergence on the southern flank  
221 of the rainfall band. Transient eddies show a significant contribution to the balance (Fig. 3d).  
222 Recall that because of the monthly resolution of the CMIP5 data, the transient eddy con-  
223 tribution is estimated from the moisture budget residual, which prevents a more careful  
224 mechanistic understanding of the transient eddy response. Changes due to winds (Fig. 3e)  
225 and temperature (Fig. 3g) are both important, with circulation changes dominating the  
226 overall spatial pattern, and temperature changes increasing moisture convergence over the  
227 climatological convergence zone. Contributions from relative humidity changes are nontriv-  
228 ial, but their magnitude and spatial extent are smaller than those from wind and temperature  
229 changes (Fig. 3f). As discussed in section 2, changes due to temperature can be decomposed  
230 into the Planck response (Fig. 3h) and the lapse rate response (Fig. 3i). The Planck response  
231 relates the climatological net precipitation, weighted by the surface warming, to changes in  
232 net precipitation, or the so-called “wet get wetter” pattern. The Planck response dominates  
233 the total response due to temperature, in both magnitude and spatial pattern. Weak signals  
234 over some land and oceanic regions are due to nearly zero climatological net precipitation,  
235 where local precipitation is primarily balanced by evaporation (c.f. Fig. 7a in Chen and  
236 Bordoni 2014). The coupling between temperature (saturation specific humidity) and wind  
237 changes (Fig. 3l) is dominant among the covariance terms (Fig. 3j-l) and resembles the dy-  
238 namic change due to only winds (Fig. 3e). The reasoning is as follows: since temperature  
239 increases everywhere, the sign in the response is due to changes in winds, with specific  
240 humidity,  $(q_s(T))$ , and specific humidity changes,  $(\delta q_s(T))$ , acting as scaling factors.<sup>1</sup>

---

<sup>1</sup>A comparison between Figs. 3 e and l shows that  $q_s(T)$  and  $\delta q_s(T)$  are of similar magnitude. This is due to the nonlinear dependence of  $q_s(T)$  on temperature, which gives rises to big changes in  $q_s(T)$  even for small changes in  $T$ . For instance, the water vapor saturation pressure is 3523 Pa at 300 K and 4701 Pa at 305 K, which implies that for only 5K difference in temperature, the water vapor saturation pressure differs

241 In both fast and slow responses, changes in circulation are significant and dominate the  
242 spatial pattern of the precipitation anomalies. Changes in thermodynamic quantities, such  
243 as temperature and relative humidity, play a less important role. Hence, we focus primarily  
244 on analyzing the local circulation changes, and infer possible mechanisms through which  
245 fundamental forcings, such as land-sea contrast, topography, and atmospheric CO<sub>2</sub>, affect  
246 local circulations directly or indirectly through larger-scale atmospheric circulation changes  
247 such as those of the NPSH.

## 248 4. Dynamic contribution to rainfall changes

249 Fig. 4 shows changes in precipitation and moisture flux due to changes in winds and  
250 geopotential height. Specifically, to clearly link geopotential height to circulation changes,  
251 in Fig. 4 we show differences in the local geopotential relative to the maximum value in  
252 the NPSH. This is because, through geostrophic balance, winds are linked to gradients in  
253 geopotential height rather than its magnitude. Additionally, geopotential heights tend to  
254 systematically shift upward under global warming. Our metric in Fig. 4 accounts for all of  
255 these factors.

256 On the larger scale, changes in the location and the strength of the NPSH in the fast  
257 response are within one standard deviation of the inter-model spread and therefore not signif-  
258 icant. In the slow response, instead, the NPSH moves southward and weakens significantly.  
259 This implies that changes in winds over the EASM region are mostly local responses in the  
260 fast response, while resulting from a combination of local and remote responses, mediated  
261 by the NPSH, in the slow response.

262 The dynamic moisture flux convergence anomalies,  $(-\langle \nabla \cdot q_0 \delta \mathbf{v} \rangle)$ , can be further de-  
263 composed into a wind convergence component,  $(-\langle q_0 \nabla \cdot \delta \mathbf{v} \rangle)$ , and an advection component,  
264  $(-\langle \delta \mathbf{v} \cdot \nabla q_0 \rangle)$ . In the following, we will analyze separately the contribution to precipitation  

---

by around 33%.

265 changes by these two terms and we will discuss possible mechanisms responsible for these  
 266 changes.

267 *a. Changes in wind convergence*

268 The wind convergence component,  $(-\langle q_0 \nabla \cdot \delta \mathbf{v} \rangle)$ , can be expressed in terms of the vertical  
 269 advection using continuity,  $-\langle \delta \omega \partial_p q_0 \rangle$ . The change in this term is largely explained by  
 270 changes in vertical velocity at 500 mb (i.e.,  $\delta \omega_{500}$ , Fig. 5).

271 The vertical velocity is directly associated with remote forcing (i.e., energy advection),  
 272 local radiative and surface fluxes, and stability. According to the MSE budget (Chen and  
 273 Bordoni 2014), vertical velocity can be approximated as the fraction between energy input  
 274 and moist static stability. Here, we define a proxy for vertical velocity at 500 mb based on  
 275 the MSE budget,

$$\omega_{500\text{apprx}} = \frac{-\langle \mathbf{v} \cdot \nabla E \rangle + F^{\text{net}}}{-\alpha \langle \partial_p h \rangle}, \quad (5)$$

276 where  $F^{\text{net}} = S_t^\downarrow - S_t^\uparrow - S_s^\downarrow + S_s^\uparrow - R_t^\uparrow + R_s^\uparrow - R_s^\downarrow + SH + LH$ ,  $h = c_p T + gz + L_v q$  is  
 277 the MSE,  $E = c_p T + L_v q$  is the atmospheric moist enthalpy, and  $F^{\text{net}}$  is the net energy  
 278 flux into the atmosphere, with the subscript  $t$  and  $s$  denoting the top of atmosphere and  
 279 surface, respectively.<sup>2</sup>  $\alpha$  is a coefficient added to account for the coupling between vertical  
 280 velocity and MSE stratification. Transient eddies are ignored and the coupling coefficient  
 281  $\alpha$  is assumed to be homogeneous for simplicity. Fig. 6 shows changes in vertical velocity as  
 282 diagnosed from the model output directly and from the approximation in Eq. A1 (i.e.,  $\delta w$   
 283 and assuming  $\alpha = 1$ ).

284 At the first order, changes in vertical velocity can be partitioned into changes in ener-  
 285 gy input and changes in stability (Appendix). Contributions from changes in energy input  
 286 (mostly from horizontal advection of moist enthalpy) are significantly larger than those from  
 287 changes in stability in both fast and slow responses (Fig. 7). In the fast response, anoma-

---

<sup>2</sup>The vertical integration of moist static energy stratification is from 700 mb to 100 mb to account for the steepest slope for stability.

288 lous positive moist enthalpy advection over Northeast China and negative moist enthalpy  
 289 advection over the climatological rainfall band are closely associated with changes in verti-  
 290 cal velocity. In the slow response, anomalies in moist enthalpy advection change sign, with  
 291 anomalous positive moist enthalpy advection over ocean and negative advection over land.  
 292 Contributions from local stability are considerably smaller, however, with a destabilizing ef-  
 293 fect over land in the fast response, and over oceanic regions in the slow response. Anomalies  
 294 in moist enthalpy advection are due to both dry enthalpy and latent energy advection, with  
 295 similar spatial pattern (not shown) because of close relationship between temperature and  
 296 water vapor changes via the Clausius-Clapeyron relationship.

297 *b. Changes in advection*

298 Changes in the advection term ( $-\langle \delta \mathbf{v} \cdot \nabla q_0 \rangle$ ) are a direct result from (mostly geostroph-  
 299 ic) wind anomalies. In the fast and slow responses, changes in local precipitation over East  
 300 China and adjacent oceanic regions are highly associated with meridional wind anomalies  
 301 (Fig. 8 b, d). Intensified (weakened) meridional wind enhances (reduces) moisture transport,  
 302 resulting in higher (lower) rainfall. In addition, the meridional component of the geostrophic  
 303 flow on a  $\beta$  plane can induce convergent flow, which reinforces local precipitation in addi-  
 304 tion to positive advective anomalies. Changes in meridional wind at 850 mb are largely  
 305 geostrophic, a consequence from changes in surface pressure gradient through geopotential  
 306 height ( $Z_{850}$ ) gradient anomalies. For simplicity, ignoring subtle influences from changes in  
 307 the atmospheric temperature between the surface and 850 mb pressure level,  $Z_{850}$  is only  
 308 dependent on  $\ln(p_s)$ , where  $p_s$  indicates surface pressure. Anomalies in locational differ-  
 309 ences in surface pressure, i.e.,  $\delta \ln(p_{s1}/p_{s2})$  change the  $Z_{850}$  gradient, and thereafter create  
 310 wind anomalies,  $\delta v_{850}$ . In the fast response, enhanced land-sea contrast is manifest in an  
 311 increased surface pressure gradient, with lower pressure over land and higher pressure over  
 312 ocean. Meridional wind is subsequently enhanced. In the slow response, however, land-sea  
 313 contrast is weakened, and the meridional wind is reduced. This relationship is well observed

314 amongst different model simulations (Fig. 9).<sup>3</sup> Changes in precipitation over the ocean-  
315 ic rainfall band, however, are largely due to changes in zonal wind, particularly in the slow  
316 response (Fig. 8 c). Enhanced lower-level westerly wind might be related to a southward dis-  
317 placement of the NPSH. In the fast response, the NPSH does not feature significant changes  
318 in its spatial pattern, which might explain why contributions from anomalous advection of  
319 climatological moisture are limited.

### 320 *c. Summary*

321 We have diagnosed precipitation changes in the EASM region in both fast and slow  
322 responses. Some robust conclusions emerging from this diagnosis include:

- 323 • Changes in net precipitation are associated with changes in the moisture flux conver-  
324 gence, which is dominated by the dynamic component (i.e., by changes in circulation);
- 325 • The wind convergence term in the dynamic component is directly linked to changes in  
326 vertical velocity through continuity;
- 327 • These changes in vertical velocity are found to be mostly related to changes in moist  
328 enthalpy advection, with changes in vertical stability playing a lesser role;
- 329 • Changes in horizontal moisture advection over East China are dominated by changes  
330 in the meridional wind, which is a consequence of changes in land-sea contrast. The  
331 zonal component dominates the slow response over the oceanic regions, as a possible  
332 consequence of the southward displacement of the NPSH.

---

<sup>3</sup>The robustness of the relationship between  $\delta \ln(p_{s1}/p_{s2})$  and  $\delta v_{850}$  is insensitive to the width of the region we choose (the East boundary varies from 130E to 140E).

## 5. Numerical simulations

We use the GFDL AM2.1 to investigate the impact of land warming and SST patterns on the EASM response to CO<sub>2</sub> forcing. We have previously shown that topography plays an essential role in the rainfall band formation (Chen and Bordoni 2014). As discussed there, the presence of topography reinforces the land-sea thermal contrast, in addition to its mechanical interactions with the prevailing flow. However, in a changing climate, can enhanced land-sea thermal contrast due to land warming alone provide a large enough forcing to cause changes in precipitation? In addition, how do changes in SST patterns affect the response of the EASM?

### *a. Land warming*

In order to expose impacts of land warming alone on the EASM, we design two experiments with changing CO<sub>2</sub> concentration in the absence of global topography: noTopo-control and noTopo-4xCO<sub>2</sub>. Fig. 10 shows the simulated precipitation change in May, June, and July with and without topography. Consistent with Chen and Bordoni (2014), in the presence of topography, a well organized rainfall band is simulated during the EASM season: the rainfall band disappears when topography is removed. In the absence of topography (Fig. 10, right), there are no significant changes in precipitation until July, when the rainfall band dissipates even in the control experiment (with topography). The difference highlights the limited impact of land warming alone on the EASM rainfall, and emphasizes the importance of topography in its response to CO<sub>2</sub> forcing.

### *b. SST patterns*

Previous literature (e.g., Xie et al. 2010) has discussed the importance of SST patterns in regional precipitation changes, arguing that the “wet get wetter” response can hold only for uniform SST changes. We illustrate the impact of spatially varying SST patterns on the

357 projected EASM rainfall by comparing the Uni4K and CMIP5SST experiments (Fig. 11).  
358 With spatially varying SSTs (Fig. 12a), rainfall increases from East China through the  
359 northwestern Pacific; rainfall instead decreases over Japan and part of the northwestern  
360 Pacific in the case of uniform SST warming (Fig. 12b). In the latter case, changes in regional  
361 net precipitation do not follow the pattern of the climatological net precipitation, as would  
362 be expected from the “wet get wetter” response.

363 Differences in rainfall projection are largely due to the dynamic component (Fig. 13) in  
364 the moisture budget. With spatially varying SSTs, the NPSH weakens and moves south-  
365 ward, which is associated with a southward displacement of the westerly jet (Fig. 12a).  
366 The weakening of the NPSH, together with its spatial displacement, creates an anomalous  
367 westerly wind to the southeast of Japan, resembling the MMM response in CMIP5 simula-  
368 tions. With uniform SST warming, the NPSH intensifies and there is little evidence of any  
369 southward displacement. As a consequence, the prevailing wind to the southeast of Japan  
370 is northeasterly, which results in a reduction in precipitation.

## 371 **6. Summary and discussion**

372 In this study, we analyzed the response of the EASM rainfall band to atmospheric CO<sub>2</sub>  
373 forcing and subsequent SST warming within the context of the moisture budget. The s-  
374 patial pattern of net precipitation changes is dominated by changes in mean moisture flux  
375 convergence, which in turn is primarily explained by changes in circulation. The thermo-  
376 dynamic component however is non-negligible; it mimics the net precipitation climatology  
377 and contributes significantly to rainfall changes under warming. Surface pressure anomalies,  
378 as a consequence of land-sea contrast due to CO<sub>2</sub> forcing, create an anomalous meridional  
379 flow over East China and adjacent oceans, which affects the moisture advection. The NPSH  
380 weakens and moves significantly southward in the slow response, creating an anomalous  
381 westerly flow to the south of the climatological rainfall band and subsequently increasing

382 moisture advection. In addition to contributions from anomalous moisture advection due to  
383 winds, anomalous wind convergence also contributes to rainfall changes. The spatial pattern  
384 is colocated with that of vertical velocity anomaly at 500 mb, which can be thought of as a  
385 response to a remote forcing, provided by anomalous horizontal moist enthalpy advection.  
386 The schematics in Fig. 14 presents the underlying mechanisms: in the fast response to CO<sub>2</sub>  
387 forcing, enhanced land-sea thermal contrast reinforces the meridional wind, which results in  
388 an increase of rainfall over East China; in the slow response, the land-sea thermal contrast  
389 is weakened because of sea surface warming, and the rainfall over East China decreases,  
390 resulting from a southward displacement of the NPSH.

391 Numerical simulations without topography show that enhanced land-sea contrast due to  
392 land warming alone cannot induce similar precipitation changes. This result implies that the  
393 land warming is not a sufficient condition for the EASM rainfall changes. It also emphasizes  
394 the important role of topography in the EASM response in terms of its climatology and  
395 climate change. In addition, spatially varying SST changes are shown to play a key role in  
396 rainfall changes in the oceanic regions through associated changes in the NPSH.

397 The fast and slow responses of the EASM to CO<sub>2</sub> forcing show an opposite pattern,  
398 implying a compensating effect in transient climate change. This result is consistent with  
399 recent work by Shaw and Voigt (2015), who highlight how changes in land-sea contrast in  
400 response to the direct radiative forcing and the indirect SST warming have an opposite  
401 impact on global circulation change. Speaking of the EASM specifically, we acknowledge the  
402 importance of land-sea contrast but emphasize the role of topography rather than that of land  
403 warming alone. Our simulations are based on GCM experiments with realistic continents,  
404 rather than the more idealized study by Shaw and Voigt (2015), who prescribe SSTs to  
405 artificially introduce land-sea contrast in their aquaplanet simulations.

406 Results emerging from this work have important implications for improving EASM pro-  
407 jections in GCMs. The dynamic component due to circulation changes, though highly model  
408 dependent and hard to constrain, can disclose mechanisms through which different forcing

409 agents influence the EASM. The thermodynamic component mimics the climatology. There-  
410 fore, a better representation of the climatological precipitation will be the first necessary step  
411 to reduce spread in regional precipitation projections. In addition, analysis of the results  
412 from the fast response highlight how dramatic changes in rainfall can occur even as a direct  
413 response to CO<sub>2</sub> forcing, without any SST warming. These changes can have a tremendous  
414 societal impact on heavily populated monsoon regions. This confirms how geo-engineering  
415 schemes that have been proposed as climate mitigation strategies and that only aim at re-  
416 ducing surface warming without CO<sub>2</sub> sequestration might have unexpected implications for  
417 the global and regional hydrological cycle (Bony et al. 2013; O’Gorman et al. 2012).

## 419 **Decomposition of the approximated vertical velocity**

420 We use  $a$ ,  $s$ , and  $w$  to represent energy input ( $-\langle \mathbf{v} \cdot \nabla E \rangle + F^{\text{net}}$ ), stability ( $\langle \partial_p h \rangle$ ) and  
 421 approximated vertical velocity at 500 mb ( $\omega_{500\text{apprx}}$ ). Therefore, Eq. 5 can be expressed  
 422 symbolically as  $w = \frac{a}{\alpha s}$ . Changes in vertical velocity ( $\delta w$ ) can be expressed as

$$\frac{\delta w}{w_0} = \frac{\delta a}{a_0} - \frac{\delta s}{s_0}, \quad (\text{A1})$$

423 where the subscript 0 indicates the control experiment, which is sstClim (sstClim4xCO2) in  
 424 the fast (slow) response. Because  $a_0$  approximates to zero in some regions, we reformulate  
 425 Eq. A1 by multiplying  $a_0$  on both sides of the equation,

$$\frac{a_0 \delta w}{w_0} = \delta a - \frac{a_0 \delta s}{s_0}. \quad (\text{A2})$$

426 One advantage of this approach is that we can avoid imposing an empirical value of  $\alpha$  while  
 427 still being able to diagnose respective contributions.

### 428 *Acknowledgments.*

429 We use the NCAR Command Language (Version 6.1.2, <http://dx.doi.org/10.5065/D6WD3XH5>)  
 430 to create the plots and analyze the data. The data analyses and simulations were conducted  
 431 on the Caltech's Division of Geological and Planetary Sciences high-performance computing  
 432 cluster.

## REFERENCES

- 435 Anderson, J., and Coauthors, 2004: The new GFDL global atmosphere and land model  
436 AM2-LM2: Evaluation with prescribed SST simulations. *J. Climate*, **17 (24)**, 4641–4673.
- 437 Bony, S., G. Bellon, D. Klocke, S. Sherwood, S. Fermepin, and S. Denvil, 2013: Robust  
438 direct effect of carbon dioxide on tropical circulation and regional precipitation. *Nature*  
439 *Geoscience*, **6 (6)**, 447–451.
- 440 Chen, J., and S. Bordoni, 2014: Orographic Effects of the Tibetan Plateau on the East Asian  
441 Summer Monsoon: An Energetic Perspective. *J. Climate*, **27 (8)**, 3052–3072.
- 442 He, C., and T. Zhou, 2015: Responses of the western north pacific subtropical high to global  
443 warming under rcp4. 5 and rcp8. 5 scenarios projected by 33 cmip5 models: The dominance  
444 of tropical indian ocean–tropical western pacific sst gradient. *Journal of Climate*, **28 (1)**,  
445 365–380.
- 446 Held, I. M., and B. J. Soden, 2006: Robust responses of the hydrological cycle to global  
447 warming. *Journal of Climate*, **19 (21)**, 5686–5699.
- 448 Kitoh, A., and T. Uchiyama, 2006: Changes in onset and withdrawal of the east  
449 asian summer rainy season by multi-model global warming experiments. *JOURNAL-*  
450 *METEOROLOGICAL SOCIETY OF JAPAN SERIES 2*, **84 (2)**, 247.
- 451 Kitoh, A., S. Yukimoto, A. Noda, and T. Motoi, 1997: Simulated changes in the asian  
452 summer monsoon at times of increased atmospheric co<sub>2</sub>. *Journal of the Meteorological*  
453 *Society of Japan*, **75 (6)**, 1019–1031.
- 454 Mitchell, J. F., C. Wilson, and W. Cunnington, 1987: On CO<sub>2</sub> climate sensitivity and model

455 dependence of results. *Quarterly Journal of the Royal Meteorological Society*, **113** (475),  
456 293–322.

457 O’Gorman, P. A., R. P. Allan, M. P. Byrne, and M. Previdi, 2012: Energetic constraints on  
458 precipitation under climate change. *Surveys in geophysics*, **33** (3-4), 585–608.

459 Shaw, T., and A. Voigt, 2015: Tug of war on summertime circulation between radiative  
460 forcing and sea surface warming. *Nature Geoscience*.

461 Smith, T. M., R. W. Reynolds, R. E. Livezey, and D. C. Stokes, 1996: Reconstruction of  
462 historical sea surface temperatures using empirical orthogonal functions. *J. Climate*, **9** (6),  
463 1403–1420.

464 Taylor, K. E., R. J. Stouffer, and G. A. Meehl, 2012: An overview of cmip5 and the experi-  
465 ment design. *Bull. Amer. Meteor. Soc.*, **93** (4), 485–498.

466 Terao, T., and T. Kubota, 2005: East-west sst contrast over the tropical oceans and the  
467 post el niño western north pacific summer monsoon. *Geophys. Res. Lett.*, **32** (15).

468 Xie, S.-P., C. Deser, G. A. Vecchi, J. Ma, H. Teng, and A. T. Wittenberg, 2010: Global  
469 warming pattern formation: sea surface temperature and rainfall\*. *Journal of Climate*,  
470 **23** (4), 966–986.

471 Xie, S.-P., K. Hu, J. Hafner, H. Tokinaga, Y. Du, G. Huang, and T. Sampe, 2009: Indian  
472 ocean capacitor effect on indo-western pacific climate during the summer following el niño.  
473 *J. Climate*, **22** (3), 730–747.

474 Yang, J., Q. Liu, S.-P. Xie, Z. Liu, and L. Wu, 2007: Impact of the indian ocean sst basin  
475 mode on the asian summer monsoon. *Geophys. Res. Lett.*, **34** (2).

476 Zhao, P., S. Yang, M. Jian, and J. Chen, 2011a: Relative controls of asian-pacific sum-  
477 mer climate by asian land and tropical-north pacific sea surface temperature. *J. Climate*,  
478 **24** (15), 4165–4188.

479 Zhao, P., S. Yang, H. Wang, and Q. Zhang, 2011b: Interdecadal relationships between the  
480 asian-pacific oscillation and summer climate anomalies over asia, north pacific, and north  
481 america during a recent 100 years. *Journal of Climate*, **24 (18)**, 4793–4799.

## 482 **List of Tables**

483	1	CMIP5 models that have outputs in piControl, sstClim, sstClim4xCO2, and	
484		abrupt4xCO2.	24
485	2	Experiments designed by using the GFDL-AM2.1.	25

TABLE 1. CMIP5 models that have outputs in piControl, sstClim, sstClim4xCO2, and abrupt4xCO2.

Model name	Modeling group	Resolution (plevXlatXlon)
bcc-csm1-1	Beijing Climate Center (BCC), China Meteorological Administration	17X64X128
CanESM2	Canadian Centre for CLimate Modelling and Analysis (CCCMA)	22X64X128
CCSM4	National Center for Atmospheric Research (NCAR)	17X192X288
CSIRO-Mk3-6-0	CSIRO in collaboration with Queensland CLimate Change Centre of Excellence (CSIRO-QCCCE)	18X96X192
inmcm4	Institute of Numerical Mathematics (INM)	17X120X180
IPSL-CM5A-LR	L’Institut Pierre-Simon Laplace (IPSL)	17X96X96
MIROC5	L’Institut Pierre-Simon Laplace (IPSL)	17X128X256
MPI-ESM-LR	Max Planck Institute for Meteorology (MPI-M)	25X96X192
MPI-ESM-MR	Max Planck Institute for Meteorology (MPI-M)	25X96X192
MRI-CGCM3	Meteorological Research Institute (MRI)	23X160X320
NorESM1-M	Norwegian Climate Centre (NCC)	17X96X144

TABLE 2. Experiments designed by using the GFDL-AM2.1.

Acronyms	Descriptions	Configurations
noTopo_control	Benchmark present-day simulation with no topography	Removed global topography, climatological SSTs, CO <sub>2</sub> concentration 320 ppm
noTopo_4xCO2	Evaluate impact on precipitation from enhanced land-sea contrast due to atmospheric CO <sub>2</sub> forcing without topographic forcing	Same as noTopo_control but with CO <sub>2</sub> concentration 1280 ppm
Topo_control	Benchmark present-day simulation with full topography	Retained global topography, climatological SSTs, CO <sub>2</sub> concentration 320 ppm
Topo_4xCO2	Evaluate impact on precipitation from enhanced land-sea contrast due to atmospheric CO <sub>2</sub> forcing with topographic forcing	Same as Topo_control but with CO <sub>2</sub> concentration 1280 ppm
Uni4K	Evaluate impact of uniform increase in SSTs by 4K	Same with 4xCO2 but global SSTs are increased by 4K everywhere
CMIP5SST	Evaluate impact of increase in SSTs as evaluated from the MMM in the CMIP5 slow response	Same as 4xCO2 but with anomalies in the slow response from CMIP5 MMM added to global SST

## 486 List of Figures

- 487 1 Multi-model mean changes in precipitation (shading,  $\text{W}/\text{m}^2$ ) between differ-  
 488 ent climate states and climatological precipitation (linear contour interval 1  
 489 mm/day, 3 – 9 mm/day) in each base state. 29
- 490 2 MMM anomalies (shading,  $\text{W}/\text{m}^2$ ) between sstClim4xCO2 and sstClim of  
 491 net precipitation  $\delta(P - E)$  (a), evaporation  $\delta E$  (b), mean flux convergence  
 492  $-\langle \delta \nabla(\mathbf{v} \cdot Hq_s) \rangle$  (c), transient component (d, subtracted from a by c), wind  
 493 component  $-\langle \nabla(\delta \mathbf{v} \cdot Hq_s) \rangle$  (e), relative humidity component  $-\langle \nabla(\mathbf{v} \cdot \delta Hq_s) \rangle$   
 494 (f), temperature component  $-\langle \nabla(\mathbf{v} \cdot H\delta q_s) \rangle$  (g), temperature component due  
 495 to the Planck response (surface temperature)  $-\alpha \delta T_s(P - E)$  (h), temperature  
 496 component due to lapse rate response (i, subtracted from g by h), covariance  
 497 between relative humidity and wind  $-\langle \nabla(\delta \mathbf{v} \cdot \delta Hq_s) \rangle$  (j), covariance between  
 498 relative humidity and temperature  $-\langle \mathbf{v} \cdot \nabla(\delta H\delta q_s) \rangle$  (k), and covariance be-  
 499 tween wind and temperature  $-\langle \nabla(\delta \mathbf{v} \cdot H\delta q_s) \rangle$  (l). Line contour (contour  
 500 interval 1 mm/day, solid (dash) line means positive (negative) value) indi-  
 501 cates climatological net precipitation in sstClim4xCO2 (a,c-l), climatological  
 502 evaporation (b). 30
- 503 3 Same with Fig. 2 but for slow response. 31
- 504 4 MMM anomalies of precipitation (shading,  $\text{W}/\text{m}^2$ ) due to winds, winds at 850  
 505 mb (vector, m/s), and difference in geopotential height between its maximum  
 506 and locational value (line contour, contour interval 30 m, solid black, purple  
 507 and brown lines indicate sstClim, sstClim4xCO2, and abrupt4xCO2, respec-  
 508 tively) at 850 mb in the fast (a) and slow (b) responses. Short dash lines in  
 509 black and purple indicate the inter-model spread (1 standard deviation) in  
 510 sstClim and sstClim4xCO2 simulations. 32

- 511 5 MMM anomalies of climatological moisture weighted wind convergence (shad-  
512 ing,  $\text{W}/\text{m}^2$ ) and vertical velocity at 500 mb (line contour, contour interval  
513  $0.005 \text{ Pa}/\text{s}$ ). Solid/dash line indicates ascending/descending motion. 33
- 514 6 MMM anomalies of approximated vertical velocity  $\omega_{500\text{apprx}}$  (Eq. A1, shad-  
515 ing,  $\text{Pa}/\text{s}$ ) and MMM anomalies of climatological vertical velocity at 500 mb  
516 (line contour, contour interval  $0.005 \text{ Pa}/\text{s}$ ). Solid/dash line indicates ascend-  
517 ing/descending motion.  $\omega_{500\text{apprx}}$  is multiplied by a factor of 2 in the fast  
518 response (a). 34
- 519 7 MMM anomalies of energy input (a and c, first term in Eq. A2, shading,  
520  $\text{W}/\text{m}^2$ ), fractional changes in stability weighted by climatological energy in-  
521 put (b and d, second term in Eq. A2, shading,  $\text{W}/\text{m}^2$ ), and climatological  
522 vertical velocity at 500 mb (line contour, contour interval  $0.005 \text{ Pa}/\text{s}$ ) in the  
523 fast (a and b) and slow (c and d) responses. Solid/dash line indicates ascend-  
524 ing/descending motions. 35
- 525 8 Zonal (a, c) and meridional (b, d) components of MMM anomalies of clima-  
526 tological moisture advection at 850 mb (shading,  $\text{W}/\text{m}^2$ ) in the fast (a, b)  
527 and slow (c, d) responses. 36
- 528 9 Scatterplot (blue/red for fast/slow reponse) of meridional wind anomaly over  
529 East China and adjacent oceans ( $25\text{N}-40\text{N}$ ,  $110\text{E}-130\text{E}$ ) and surface pressure  
530 gradient anomaly between land ( $100\text{E}-120\text{E}$ ) and ocean ( $130\text{E}-150\text{E}$ ) over  
531  $25\text{N}-40\text{N}$  band. Each dot represents one model output as indicated in Table 1.  
532 Solid line indicates linear regression line in fast/slow response, respectively.  
533 See text for more details. 37
- 534 10 GFDL AM2.1 simulations of precipitation (shading,  $\text{W}/\text{m}^2$ ) in the fast re-  
535 sponse with full topography (left) and without topography (right) in May  
536 (a,b), June (c,d), and July (e,f). Line contour (contour interval  $1 \text{ mm}/\text{day}$ ,  $3$   
537  $- 9 \text{ mm}/\text{day}$ ) indicates climatological precipitation in each comparison. 38

- 538 11 GFDL AM2.1 simulations of precipitation in June (shading,  $\text{W}/\text{m}^2$ ) with  
539 CMIP5 anomalous SST pattern (a) and with 4K uniform SST increase (b).  
540 Line contour (contour interval 1 mm/day, 3 – 9 mm/day) indicates climato-  
541 logical precipitation. 39
- 542 12 GFDL AM2.1 simulations of surface temperature (shading,  $\text{W}/\text{m}^2$ ), 850 mb  
543 winds (vector) and the westerly core (maximum westerly wind, black indicates  
544 climatology, purple and blue indicate simulations with CMIP5 anomalous SST  
545 pattern and 4K uniform SST increase, respectively) with CMIP5 anomalous  
546 SST pattern (a) and with 4K uniform SST increase (b). 40
- 547 13 GFDL AM2.1 simulations of net precipitation (a-c), evaporation (d-f), wind  
548 component (g-i), relative humidity component (j-l) and temperature compo-  
549 nent (m-o) as in Fig. 2 for fast response (left), slow response (middle), and slow  
550 response with uniform 4K increase in SSTs (right) with full topography. Line  
551 contour (contour interval 1 mm/day, 3 – 9 mm/day) indicates climatological  
552 precipitation in each comparison. 41
- 553 14 Schematic of the fast and slow responses of the EASM to  $\text{CO}_2$  forcing. Red  
554 oval represents the TP and dashed line indicates the NPSH. 42

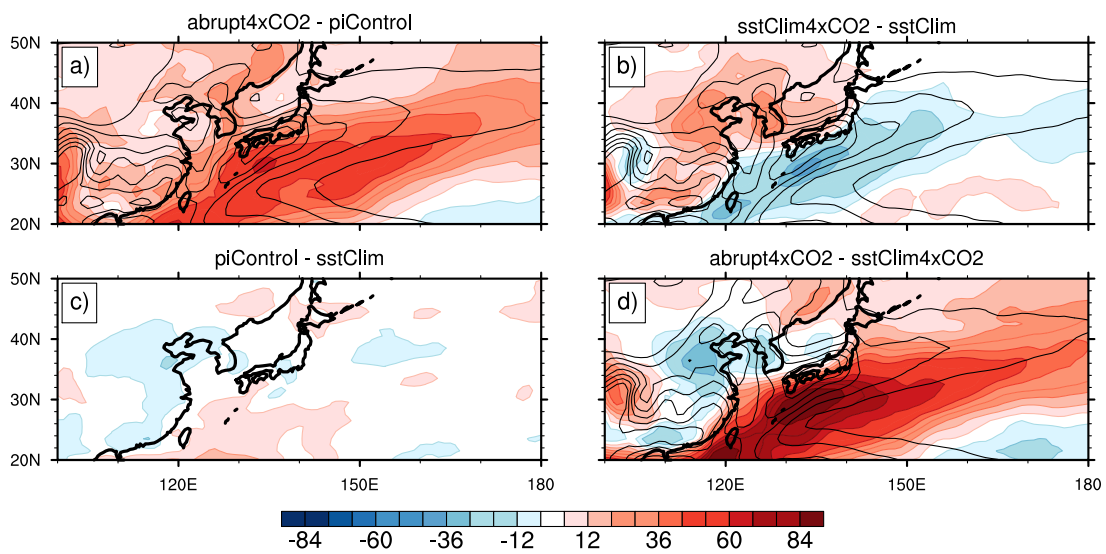


FIG. 1. Multi-model mean changes in precipitation (shading,  $W/m^2$ ) between different climate states and climatological precipitation (linear contour interval 1 mm/day, 3 – 9 mm/day) in each base state.

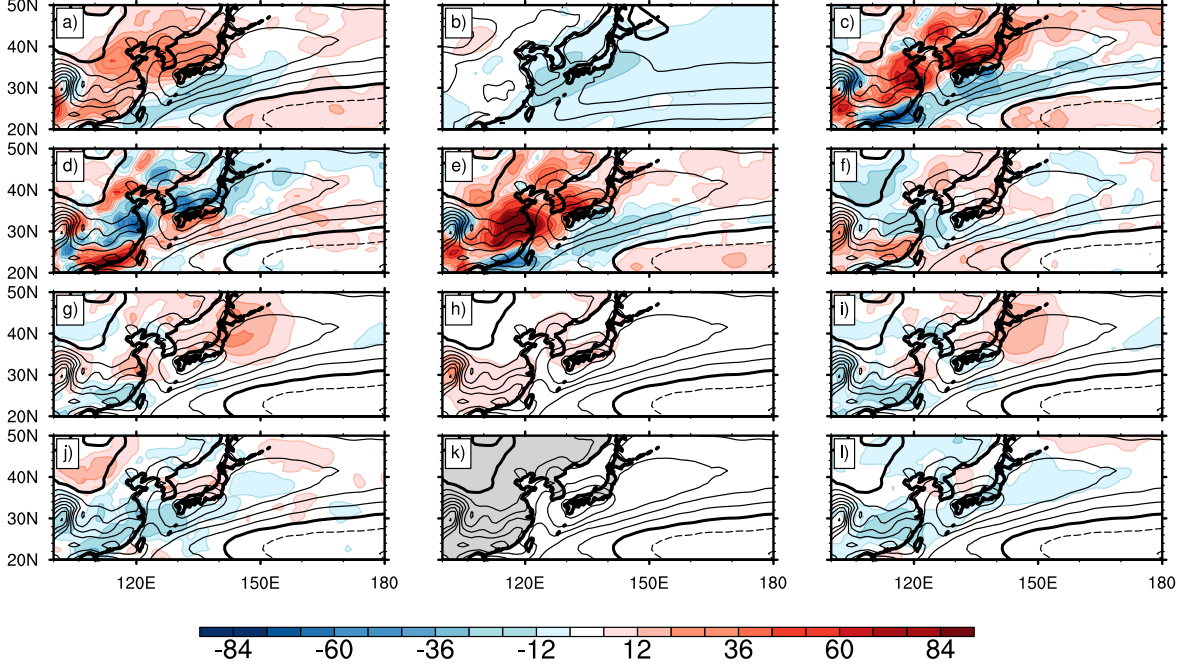


FIG. 2. MMM anomalies (shading,  $\text{W/m}^2$ ) between  $\text{sstClim4xCO}_2$  and  $\text{sstClim}$  of net precipitation  $\delta(P - E)$  (a), evaporation  $\delta E$  (b), mean flux convergence  $-\langle \delta \nabla(\mathbf{v} \cdot Hq_s) \rangle$  (c), transient component (d, subtracted from a by c), wind component  $-\langle \nabla(\delta \mathbf{v} \cdot Hq_s) \rangle$  (e), relative humidity component  $-\langle \nabla(\mathbf{v} \cdot \delta Hq_s) \rangle$  (f), temperature component  $-\langle \nabla(\mathbf{v} \cdot H\delta q_s) \rangle$  (g), temperature component due to the Planck response (surface temperature)  $-\alpha \delta T_s(P - E)$  (h), temperature component due to lapse rate response (i, subtracted from g by h), covariance between relative humidity and wind  $-\langle \nabla(\delta \mathbf{v} \cdot \delta Hq_s) \rangle$  (j), covariance between relative humidity and temperature  $-\langle \mathbf{v} \cdot \nabla(\delta H\delta q_s) \rangle$  (k), and covariance between wind and temperature  $-\langle \nabla(\delta \mathbf{v} \cdot H\delta q_s) \rangle$  (l). Line contour (contour interval 1 mm/day, solid (dash) line means positive (negative) value) indicates climatological net precipitation in  $\text{sstClim4xCO}_2$  (a,c-l), climatological evaporation (b).

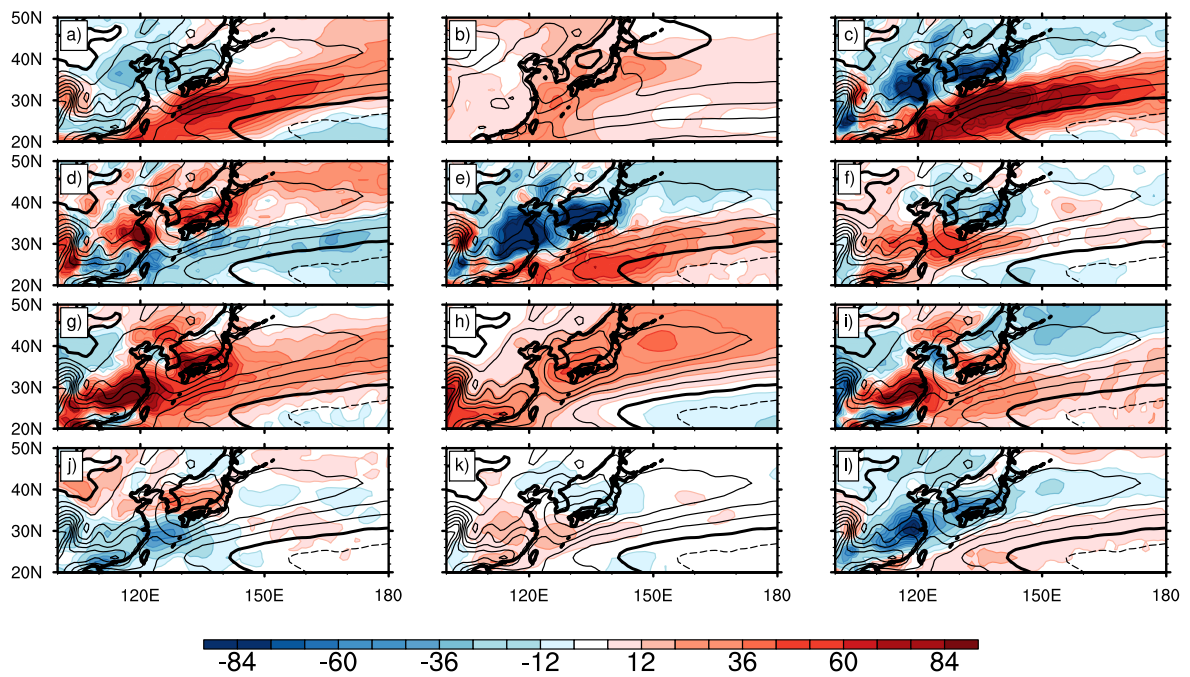


FIG. 3. Same with Fig. 2 but for slow response.

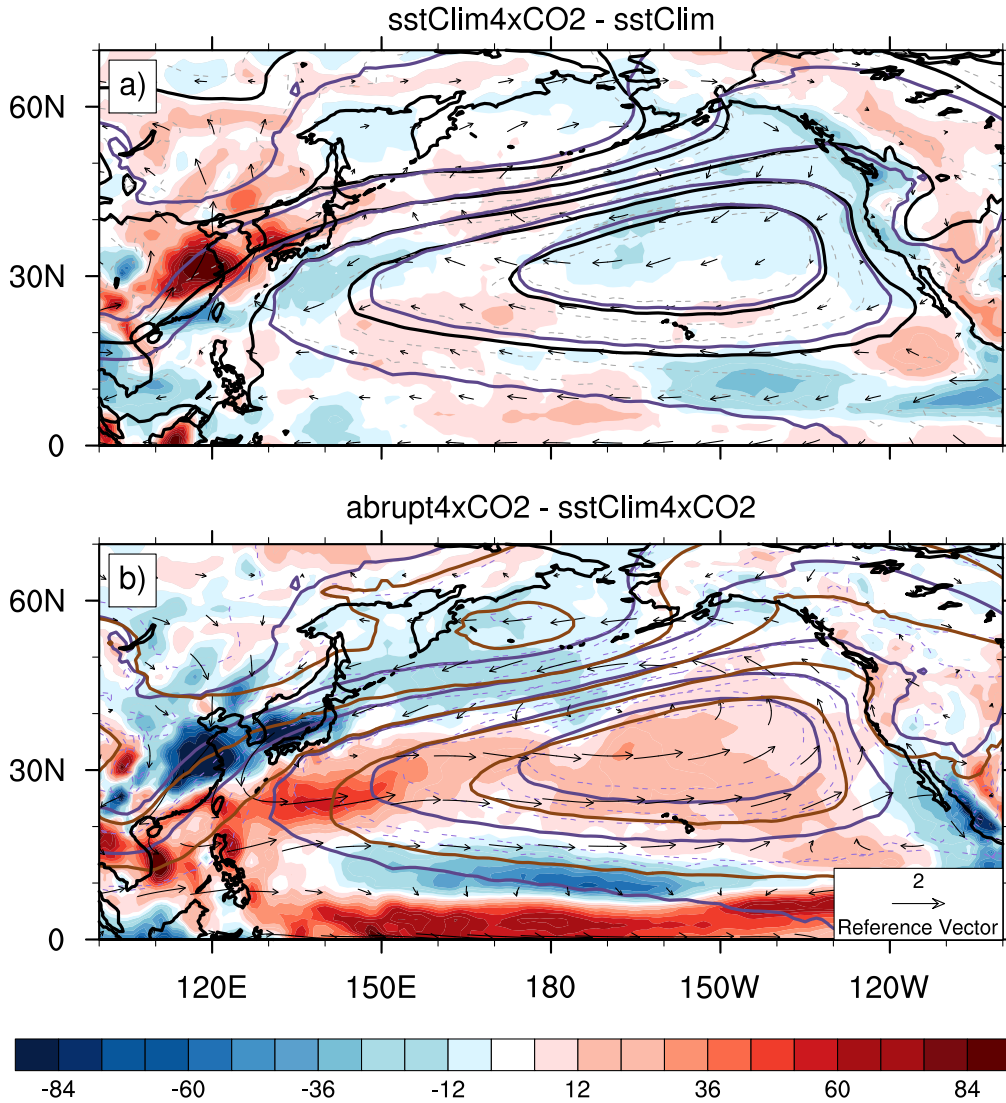


FIG. 4. MMM anomalies of precipitation (shading,  $\text{W}/\text{m}^2$ ) due to winds, winds at 850 mb (vector,  $\text{m}/\text{s}$ ), and difference in geopotential height between its maximum and locational value (line contour, contour interval 30 m, solid black, purple and brown lines indicate sstClim, sstClim4xCO2, and abrupt4xCO2, respectively) at 850 mb in the fast (a) and slow (b) responses. Short dash lines in black and purple indicate the inter-model spread (1 standard deviation) in sstClim and sstClim4xCO2 simulations.

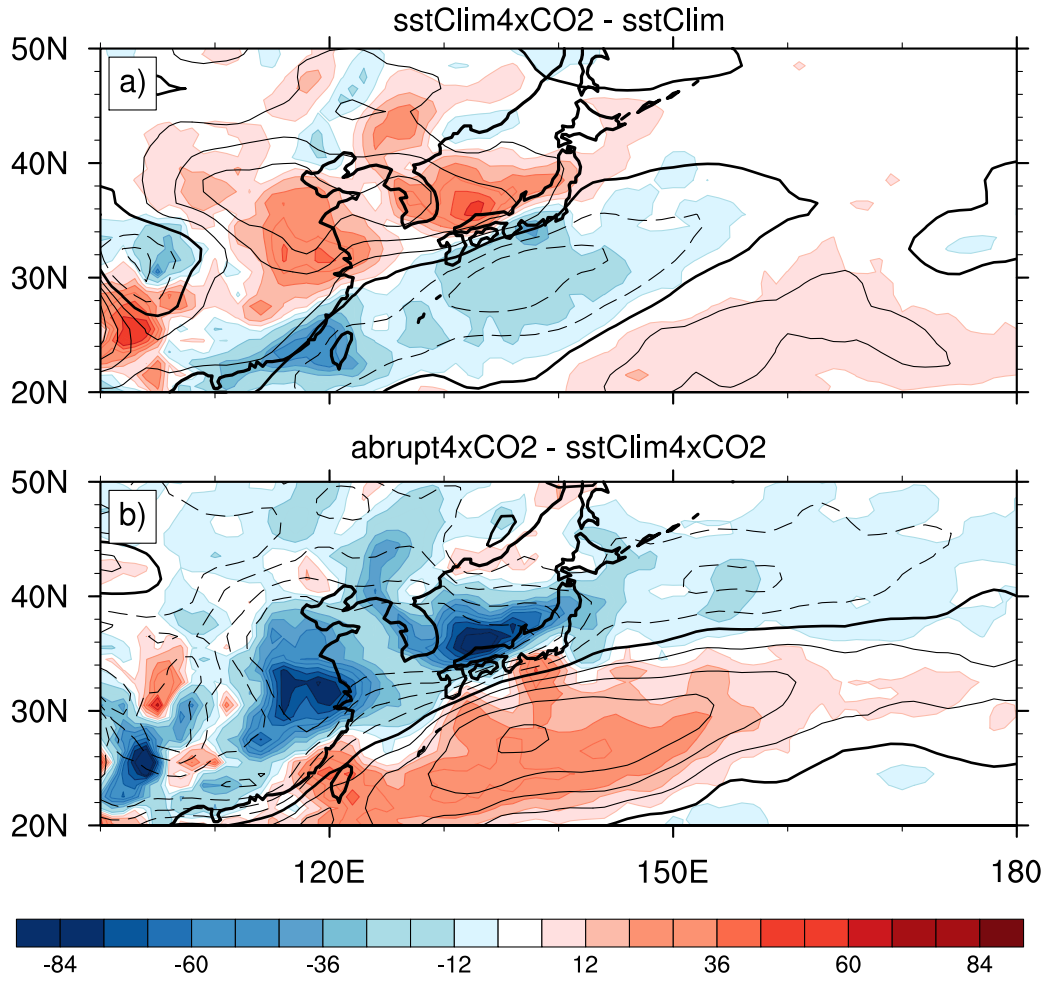


FIG. 5. MMM anomalies of climatological moisture weighted wind convergence (shading,  $W/m^2$ ) and vertical velocity at 500 mb (line contour, contour interval 0.005  $Pa/s$ ). Solid/dash line indicates ascending/descending motion.

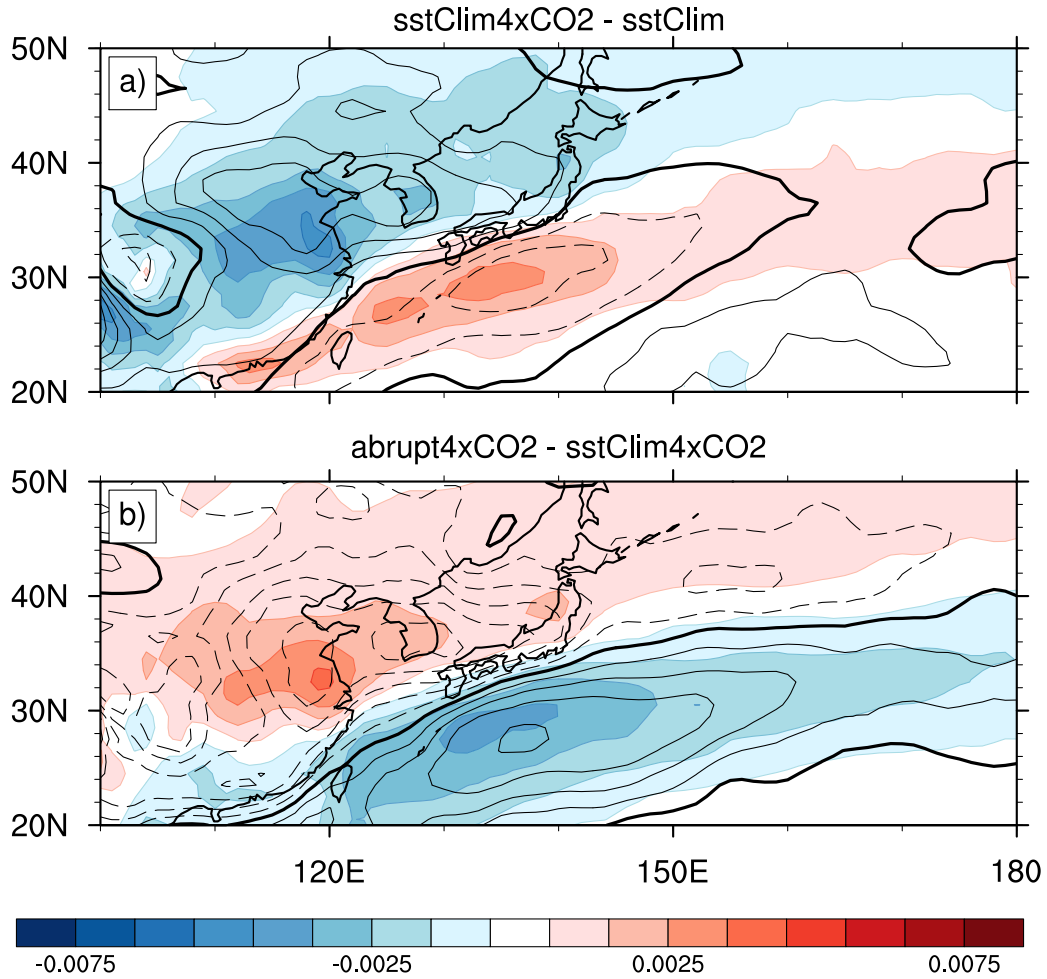


FIG. 6. MMM anomalies of approximated vertical velocity  $\omega_{500\text{apprx}}$  (Eq. A1, shading, Pa/s) and MMM anomalies of climatological vertical velocity at 500 mb (line contour, contour interval 0.005 Pa/s). Solid/dash line indicates ascending/descending motion.  $\omega_{500\text{apprx}}$  is multiplied by a factor of 2 in the fast response (a).

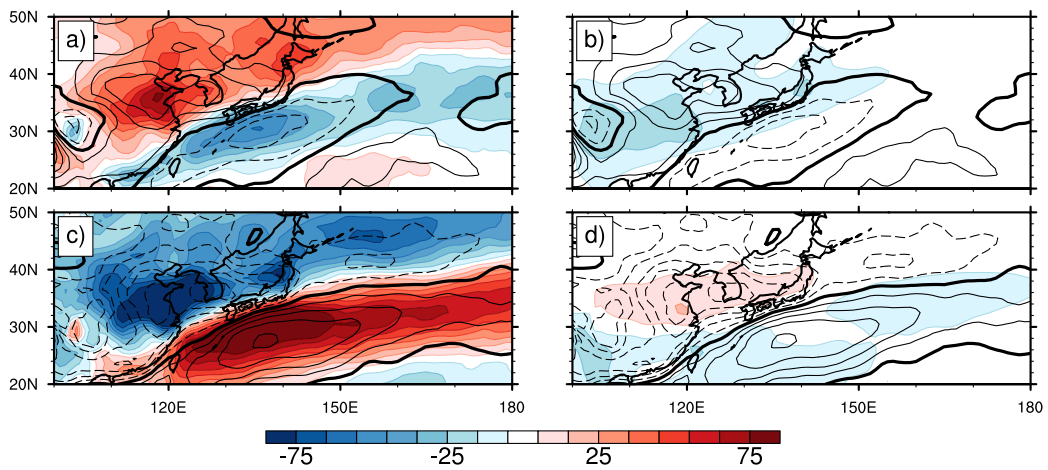


FIG. 7. MMM anomalies of energy input (a and c, first term in Eq. A2, shading,  $\text{W/m}^2$ ), fractional changes in stability weighted by climatological energy input (b and d, second term in Eq. A2, shading,  $\text{W/m}^2$ ), and climatological vertical velocity at 500 mb (line contour, contour interval  $0.005 \text{ Pa/s}$ ) in the fast (a and b) and slow (c and d) responses. Solid/dash line indicates ascending/descending motions.

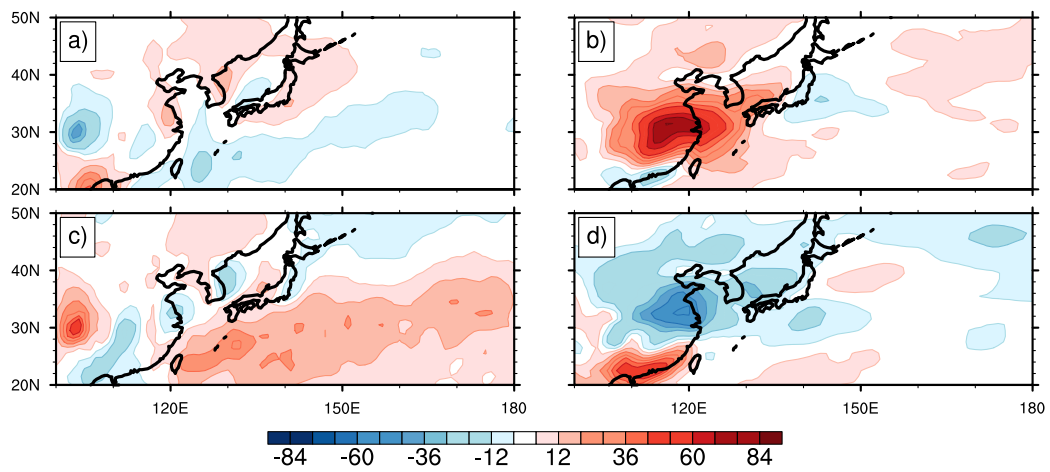


FIG. 8. Zonal (a, c) and meridional (b, d) components of MMM anomalies of climatological moisture advection at 850 mb (shading,  $W/m^2$ ) in the fast (a, b) and slow (c, d) responses.

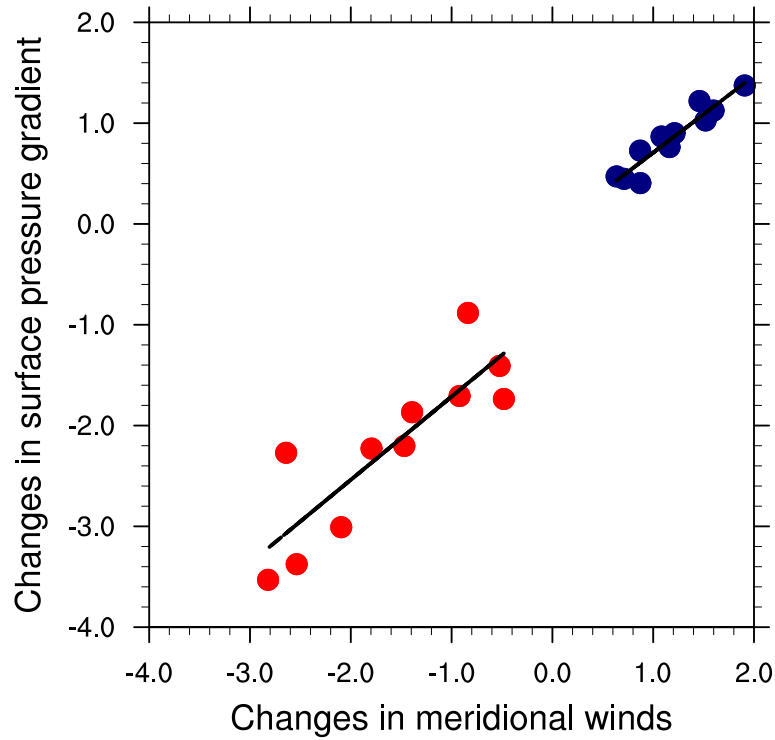


FIG. 9. Scatterplot (blue/red for fast/slow reponse) of meridional wind anomaly over East China and adjacent oceans (25N-40N, 110E-130E) and surface pressure gradient anomaly between land (100E-120E) and ocean (130E-150E) over 25N-40N band. Each dot represents one model output as indicated in Table 1. Solid line indicates linear regression line in fast/slow response, respectively. See text for more details.

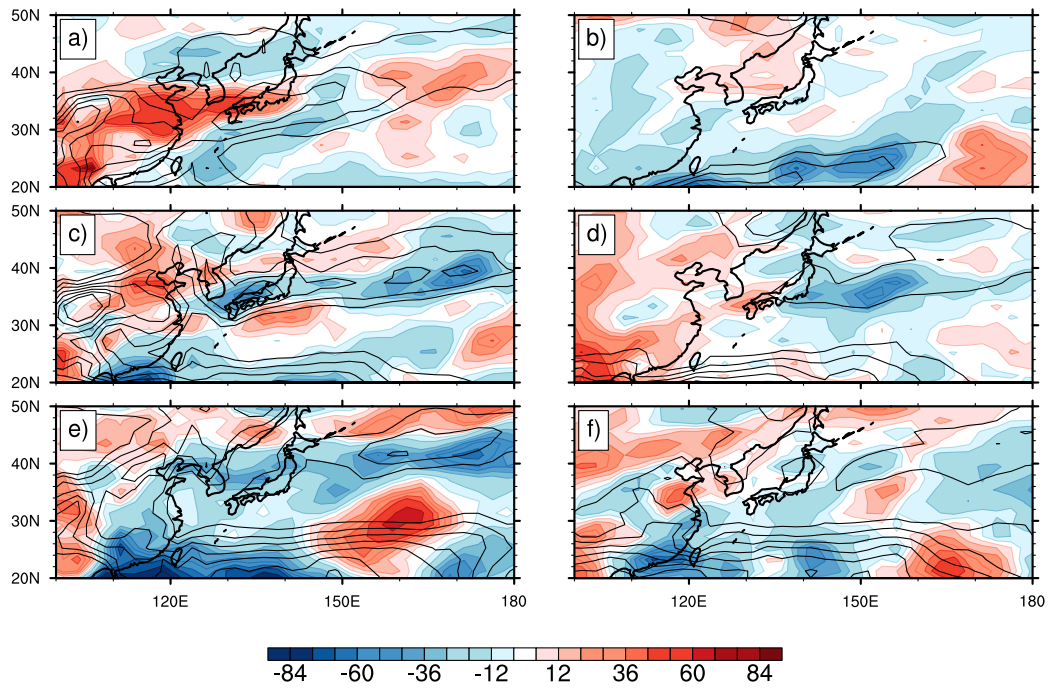


FIG. 10. GFDL AM2.1 simulations of precipitation (shading,  $\text{W}/\text{m}^2$ ) in the fast response with full topography (left) and without topography (right) in May (a,b), June (c,d), and July (e,f). Line contour (contour interval 1 mm/day, 3 – 9 mm/day) indicates climatological precipitation in each comparison.

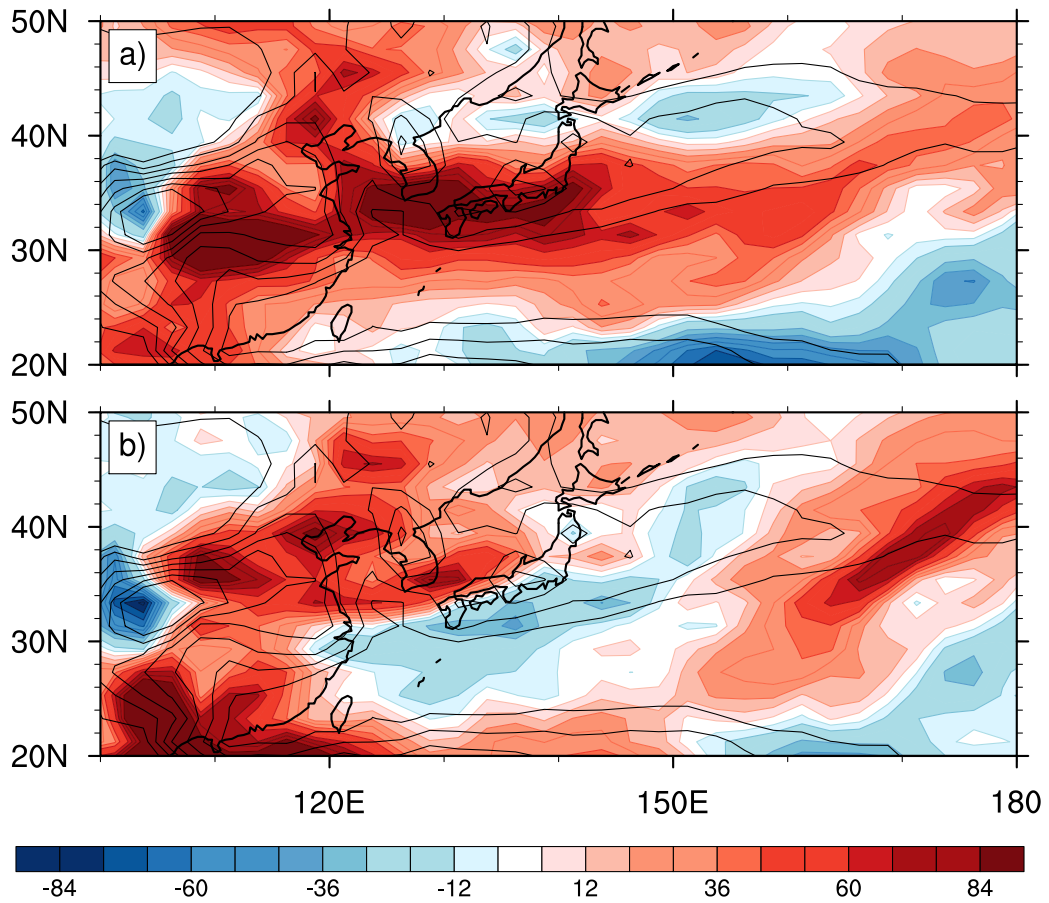


FIG. 11. GFDL AM2.1 simulations of precipitation in June (shading,  $W/m^2$ ) with CMIP5 anomalous SST pattern (a) and with 4K uniform SST increase (b). Line contour (contour interval 1 mm/day, 3 – 9 mm/day) indicates climatological precipitation.

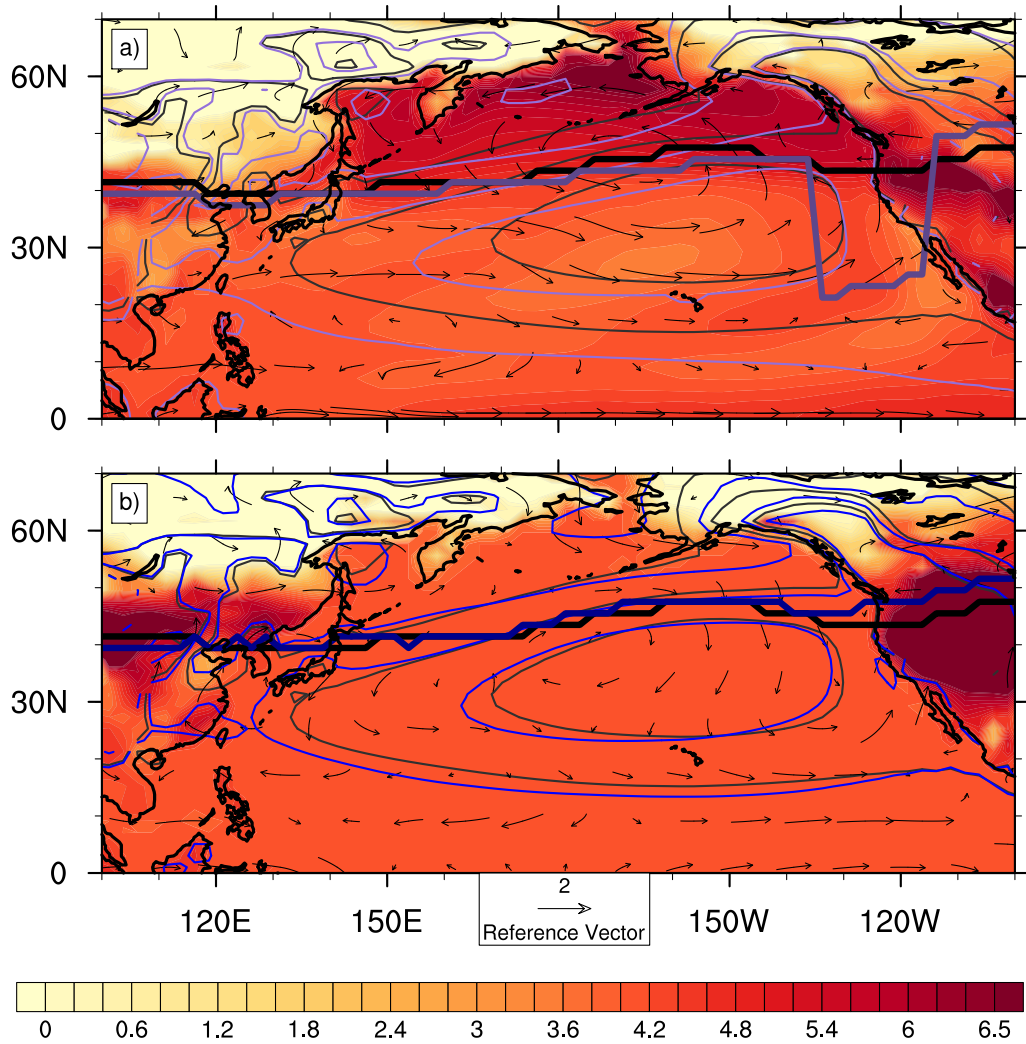


FIG. 12. GFDL AM2.1 simulations of surface temperature (shading,  $W/m^2$ ), 850 mb winds (vector) and the westerly core (maximum westerly wind, black indicates climatology, purple and blue indicate simulations with CMIP5 anomalous SST pattern and 4K uniform SST increase, respectively) with CMIP5 anomalous SST pattern (a) and with 4K uniform SST increase (b).

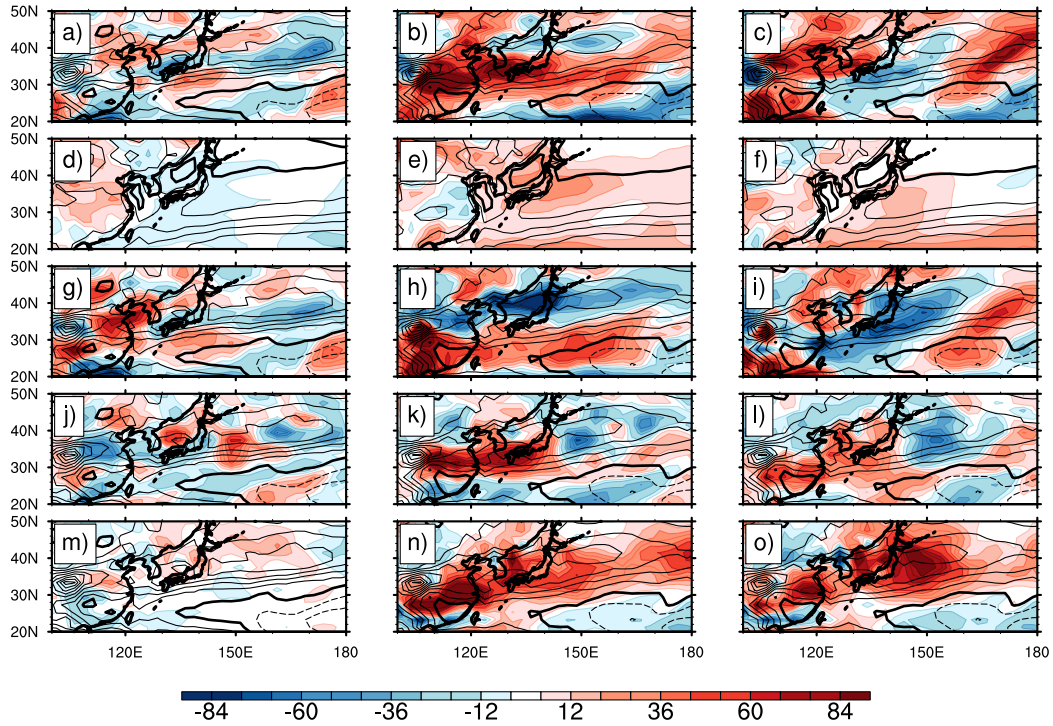


FIG. 13. GFDL AM2.1 simulations of net precipitation (a-c), evaporation (d-f), wind component (g-i), relative humidity component (j-l) and temperature component (m-o) as in Fig. 2 for fast response (left), slow response (middle), and slow response with uniform 4K increase in SSTs (right) with full topography. Line contour (contour interval 1 mm/day, 3 – 9 mm/day) indicates climatological precipitation in each comparison.

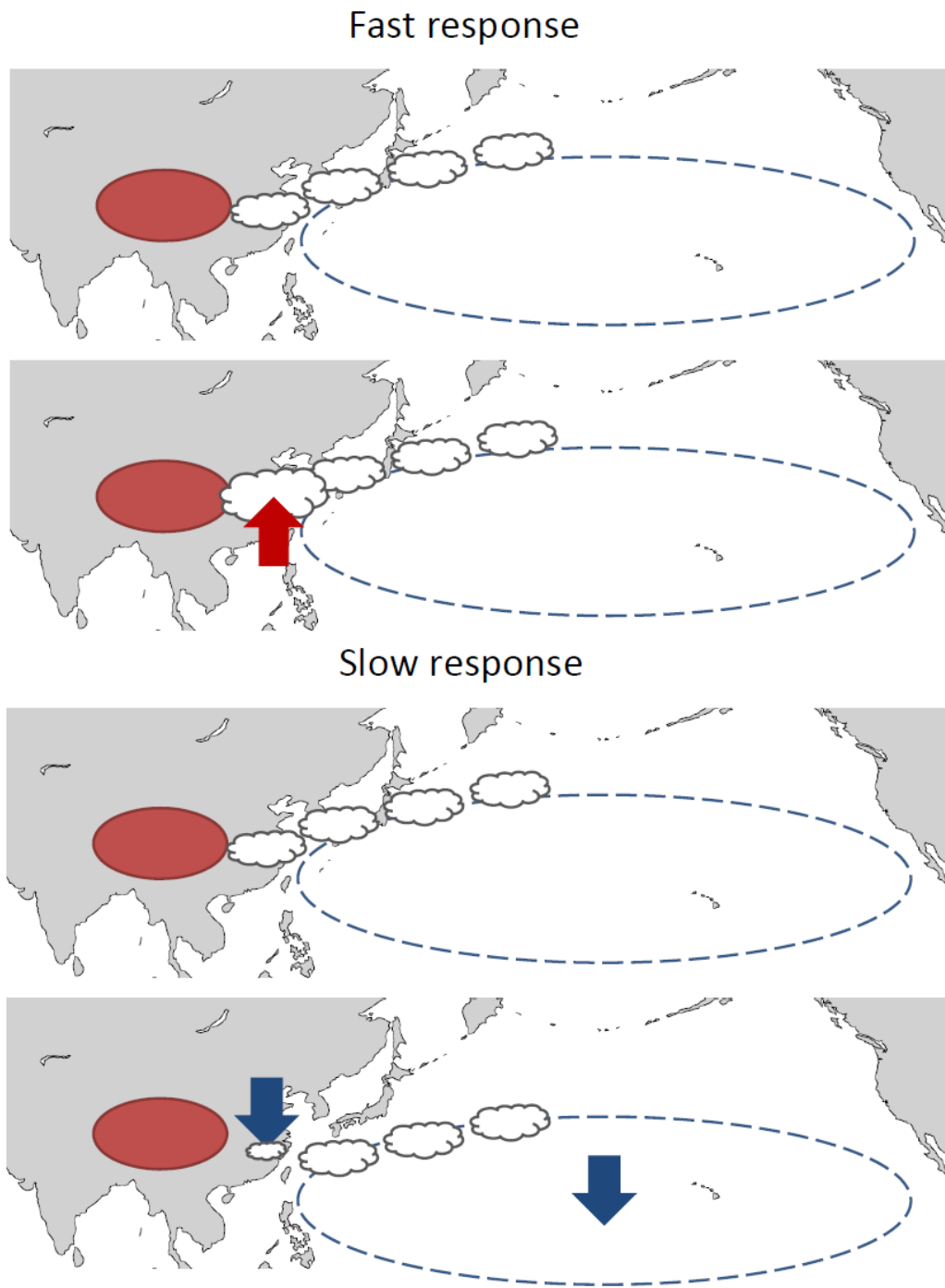


FIG. 14. Schematic of the fast and slow responses of the EASM to  $\text{CO}_2$  forcing. Red oval represents the TP and dashed line indicates the NPSH.